

# **A Surface Energy Balance Model for Predicting Temperature Evolution of Random-Shaped Smoldering Objects in Open Environments**

Saurabh Saxena, Neda Yaghoobian\*

Florida State University, FAMU-FSU College of Engineering, Department of Mechanical Engineering, Tallahassee, FL, USA

## **Abstract**

In this paper, a new computational model, Temperature Evolution of Random-shaped Smoldering Objects (TERSO), is developed to predict the temperature evolution of objects with any complex shapes under variable environmental conditions. The model is applicable to natural and manmade random-shaped objects (or a collection of objects) in an open atmosphere under the influence of local diurnal solar radiation and/or smoldering heat. In this regard, a detailed surface energy balance analysis is performed in high spatiotemporal resolution over three-dimensional objects of any shape. The model performance was validated against several existing measured data in the literature. TERSO provides temperature modeling capabilities for several applications that involve arbitrary-shaped objects of any size, whether smoldering or non-smoldering, that are hanging (e.g., fruits), in-flight (e.g., firebrands), or surface-mounted (e.g., buildings). The discrete, high-resolution surface temperature information obtained from the model can also provide unsteady thermal boundary conditions for computational fluid dynamics simulations when coupled physics is desired.

**Keywords:** Diurnal surface temperature, Fire, Radiative exchanges, Smoldering, View Factor

## **1. Introduction**

Monitoring spatiotemporal variation of surface temperatures of objects or structures in open environments requires local measurements that can be done using appropriate tools. However, conducting local measurements, especially in transient and unsteady conditions under variable forces, can be challenging and its feasibility depends on the scale of the structure/s under consideration. Accurate computational simulation of transient surface temperatures, on the other hand, requires detailed energy balance analyses in high spatial and temporal resolutions, which is challenging, especially for random-shaped multi-material complex objects. The majority of the existing computational models that perform surface energy balance analysis are introduced in the

field of urban microclimatology, where the objects under investigation are mainly simple-shaped surface-mounted cubes or two-dimensional rectangles, representing buildings. Some examples are the models developed by Arnfield (1990), Wu (1995, URBAN 4), Mills (1997), Kanda et al. (2005, SUMM), Krayenhoff & Voogt (2007, TUF-3D), Yaghoobian & Kleissl (2012, TUF-IOBES), Asawa et al. (2008), Hénon et al. (2012, SOLENE), Liu et al. (2012), Yang & Li (2013, MUST), and Lee & Lee (2020, MUSE). In some of these models, the imposed environmental condition was steady-state and thus, did not represent the transient forcing due to the variable radiative conditions (e.g., Arnfield 1990), the incident radiation was prescribed based on empirical relationships with constant values of solar intensity (e.g. Wu 1995; Mills 1997; Yang & Li 2013), the whole urban region was made of one uniform material (e.g., Arnfield 1990; Kanda et al. 2005), or only a bulk-value surface temperature was simulated for an entire building façade, ignoring sub-facet scale temperatures and the transient shadow effects (e.g., Mills 1997; Kanda et al. 2005). There have been a few conduction-only-based studies that handle more complex non-cubic objects (such as trapezoids, semicircular enclosures, and three-dimensional (3D) kidney-shaped structures (Baek et al. 1998; Kim et al. 2001; Byun et al. 2003; Zabihi et al. 2017)). However, these simple models do not fall in the category of transient-environment models that perform surface energy balance analysis as they only provide the internal-body temperature of the objects due to conduction as a result of prescribed fixed surface temperatures.

To the best of our knowledge, currently, there exists no model capable of simulating the temperature evolution of objects/fuels prior, during, and after smoldering. This is particularly important in the wildfire-propagation research and for determining *when* an object reaches its burning/smoldering point, *how* it smolders, and for *how long* it carries its high energy. All these stages of pre- to post-smoldering conditions depend on the fuel properties and local environmental forces, which are variable due to the variable solar radiation and local wind felt on the surface of the object. This work presents the development of a novel model, Temperature Evolution of Random-shaped Smoldering Objects (TERS0). TERS0 can perform surface energy balance analysis in high spatial resolution and across time scales of seconds to days to predict surface and body temperature evolution of objects with any shape (see some examples in Fig. 1) and size and with non-uniform material properties under changing environmental conditions and/or smoldering heat. The work presents the model theory and demonstrates that TERS0 performs well relative to

available observations. Description of the model is provided in Sect. 2, followed by three full-model validation studies in Sect. 3, and the conclusion.

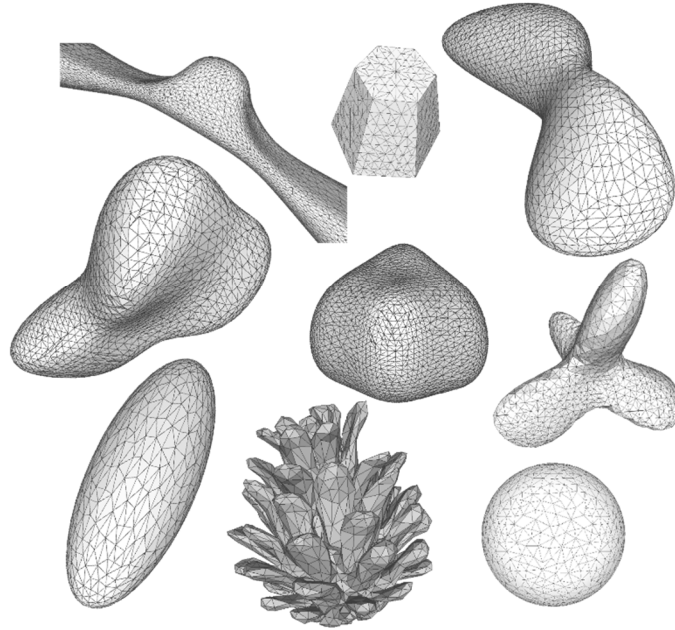


Figure 1: A few examples of random-shaped objects that can be used in TERSO (the ability of TERSO in predicting temperature evolution is not limited to these examples).

## 2. Model Design

### 2.1 Handling Complex Geometry and the Energy Budget Equation

In TERSO, 3D complex random-shaped objects are modeled by defining triangular mesh patches over the objects' surfaces. Each surface patch is defined by its vertex coordinates that form the face of the patch and an outward vector normal to the face. Individual patch orientation is specified by its normal with no restrictions to the direction, which permits the model to handle any complex surface. Each patch is in instantaneous energy exchange with its immediate environment and surrounding patches/objects. The modeled objects can be surface-mounted or non-surface-mounted (e.g., hanging or flying). The energy balance calculations are performed over each individual triangular patch, providing a high-resolution prediction of an object's surface temperature evolution. The energy balance calculation is done by considering the geographical location of the object (allowing for the accurate calculation of diurnal solar position and flux), local (minute or hourly) weather conditions provided by the typical meteorological year (TMY)

weather data files, and characteristics of the surface and substrate materials of each patch defined by their thermal and radiative properties. TMY files provide meteorological data for typical days of a typical year in different geographical locations. The fundamental formula for the energy equilibrium at a triangular patch  $i$  (Eq. (1)) includes net radiative heat exchanges ( $R_{net,i}$  (W)) comprising of net shortwave ( $R_{SW,net,i}$  (W)) and net longwave ( $R_{LW,net,i}$  (W)) radiations absorbed over the patch, convective heat exchanges at the patch surface including sensible ( $Q_{H,i}$  (W)) and latent ( $Q_{E,i}$  (W)) heat, and one-dimensional (1D) conduction of heat ( $Q_{G,i}$  (W)) normal to the patch material layers. In the case of smoldering objects, the heat input due to smoldering ( $Q_{F,i}$  (W)) is also considered. Each of these terms is described in the following subsections.

$$R_{net,i} = Q_{G,i} + Q_{H,i} + Q_{E,i} + Q_{F,i} \quad (1)$$

Equation (1) is a fourth-order equation that is solved for the surface temperature of patch  $i$  ( $T(i, t)$  (K)) at each time step ( $t$ ) using the Newton-Raphson method until the patch surface temperature varies less than 0.001K between iterations. For simplicity,  $T(i, t)$  will be represented as  $T_i$  in the following.

## 2.2 Net Radiative Heat Exchange Rate

The net radiative heat exchanges represent a combination of shortwave and longwave radiations (Eq. (2)) received over a surface and reflected/emitted by it, each of which is detailed below.

$$R_{net,i} = R_{SW,net,i} + R_{LW,net,i} \quad (2)$$

### 2.2.1 Net Shortwave Radiation

The quantity of shortwave radiation that is received by each patch is a function of the sun's position, the orientation of the patch with respect to the sun, the presence of any obstructions between the sun and the patch, and the flux of direct solar radiation and diffuse shortwave radiation from the environment and other patches. The obstructions, if any, determine the shaded regions, which are established using the shadow model described in Sect. 2.2.4. The net shortwave radiation received over patch  $i$  is, therefore, calculated using:

$$R_{SW,net,i} = R_{SW,i} \downarrow - R_{SW,i} \uparrow \quad (3).$$

$R_{SW,i} \downarrow (W)$  is the total downwelling shortwave radiation received by the patch and  $R_{SW,i} \uparrow (W)$  is the total upwelling shortwave radiation reflected by the patch, defined, respectively, by Eq. (4) and (5):

$$R_{SW,i} \downarrow = R_{SW,direct,i} + R_{SW,diffuse,i} + \sum_{m=1}^{threshold} \sum_{j=1}^{npatch} F_{ji} (R_{SW,j}^{m-1} \uparrow) \quad (4),$$

$$R_{SW,i} \uparrow = a_i R_{SW,i} \downarrow \quad (5).$$

In Eq. (4),  $R_{SW,direct,i} (W)$  is the incident direct solar radiation and  $R_{SW,diffuse,i} (W)$  is the incident diffuse shortwave radiation (defined, respectively, in Eq. (9) and (10)), and the last term is the summation of the shortwave radiation reflected from other surrounding patches received over patch  $i$ .  $npatch$  is the total number of patches in the domain. Each patch experiences multiple reflections with  $m$  being the reflection number. Reflections are computed until the remaining unabsorbed radiation is below a user-defined threshold or until a minimum user-defined number of reflections is achieved (represented in the term *threshold*).  $a_i$  in Eq. (5) is the patch surface albedo, which depends on the patch surface material and determines the amount of shortwave radiation reflected by the surface back to the environment.

Equation (6) details the total upwelling shortwave reflection from patch  $i$ .  $R_{SW,i} \uparrow$  includes the initial reflected shortwave radiation ( $R_{SW,i}^0 \uparrow (W)$ ) and other subsequent reflections ( $R_{SW,i}^m \uparrow (W)$ ) from the patch. The initial reflection ( $R_{SW,i}^0 \uparrow (W)$ ; Eq. (7)) is the sum of the reflected fractions of the incident direct solar and diffuse shortwave radiations. Subsequent reflections ( $R_{SW,i}^m \uparrow (W)$ ; Eq. (8)) are fractions of the previous reflections from other surrounding patches  $j$ , allowing for the consideration of multiple reflections in the model.

$$R_{SW,i} \uparrow = R_{SW,i}^0 \uparrow + \sum_{m=1}^{threshold} (R_{SW,i}^m \uparrow) \quad (6),$$

$$R_{SW,i}^0 \uparrow = a_i R_{SW,direct,i} + a_i R_{SW,diffuse,i} \quad (7),$$

$$R_{SW,i}^m \uparrow = a_i \sum_{j=1}^{npatch} F_{ji} (R_{SW,j}^{m-1} \uparrow) \quad (8).$$

The incident direct solar and diffuse shortwave radiations in Eq. (4) are found from:

$$R_{SW,direct,i} = \mathbf{n}_i \cdot \mathbf{R} A_i \quad (9),$$

$$R_{SW,diffuse,i} = \left( 1 - \sum_{j=1}^{npatch} F_{ij} \right) \cdot I_{diffuse} A_i \quad (10).$$

In Eq. (9),  $\mathbf{R}$  ( $= |I_{direct}| \mathbf{r}_{unit}$ ) is the solar radiation vector with  $\mathbf{r}_{unit}$  being the solar unit vector.  $I_{direct}$  ( $\text{W m}^{-2}$ ) is the flux of incident direct solar radiation at a particular time for a particular geographical location that is obtained from available weather data files.  $A_i$  ( $\text{m}^2$ ) is the area of the patch and  $\mathbf{n}_i$  is the area normal outward unit vector. In Eq. (10),  $I_{diffuse}$  ( $\text{W m}^{-2}$ ) is the flux of incident diffuse solar radiation of the location attained from available weather data files,  $F_{ij}$  is the view factor of patch  $i$  with respect to patch  $j$  (explained in Sect. 2.2.3), and thus correspondingly  $(1 - \sum_{j=1}^{npatch} F_{ij})$  is the sky view factor of patch  $i$ .

To calculate the solar unit vector ( $\mathbf{r}_{unit}$ ), we first determine the solar position (i.e., solar azimuth ( $\phi$ ) and solar zenith ( $Z$ ) angles) following the National Oceanic and Atmospheric Administration (NOAA) solar position calculator (NOAA 2018), for which the latitude, longitude, date, and time zone of the location under consideration is required. The implementation of the NOAA solar position equations in this model has been verified for two locations (Vancouver, Canada and Guerville, France) with excellent accuracy. The solar unit vector is then estimated from Eq. (11):

$$\mathbf{r}_{unit} = \cos(\phi) \sin(Z) \mathbf{e}_x - \sin(\phi) \sin(Z) \mathbf{e}_y + \cos(Z) \mathbf{e}_z \quad (11),$$

in which  $\mathbf{e}_x$ ,  $\mathbf{e}_y$ , and  $\mathbf{e}_z$  are unit vectors pointing towards the geographical north, west, and vertical directions, respectively.

### 2.2.2 Net Longwave Radiation

In a similar manner to shortwave radiation, the rate of longwave radiative heat received over a patch surface is calculated using the following equations:

$$R_{LW,net,i} = R_{LW,i} \downarrow - R_{LW,i} \uparrow \quad (12)$$

$$R_{LW,i} \downarrow = R_{LW,sky,i} + \sum_{m=1}^{threshold} \sum_{j=1}^{npatch} F_{ji} (R_{LW,j}^{m-1} \uparrow) \quad (13)$$

$$R_{LW,sky,i} = \left( 1 - \sum_{j=1}^{npatch} F_{ij} \right) \sigma T_{sky}^4 A_i \quad (14).$$

Here,  $R_{LW,i} \downarrow (W)$  is the total downwelling longwave radiation received by patch  $i$  and  $R_{LW,i} \uparrow (W)$  is the total upwelling longwave radiation emitted by it. In Eq. (13),  $R_{LW,sky,i} (W)$  is the incident longwave radiation from the sky and the last term is the summation of the longwave radiation reflected/emitted from all other surrounding patches received over patch  $i$ .  $T_{sky} (K)$  is the measured air temperature (obtained from weather data files) and  $\sigma = 5.67 \times 10^{-8} (kg s^{-3} K^{-4})$  is the Stefan-Boltzmann constant.

The total upwelling longwave radiation from patch  $i$  ( $R_{LW,i} \uparrow (W)$ , see Eq. (15)) is divided into the emitted longwave radiation by the patch due to its surface temperature ( $R_{LW,i}^0 \uparrow (W)$ , Eq. (16)), the first reflected longwave radiation from the patch ( $R_{LW,i}^1 \uparrow (W)$ , Eq. (17)), and other subsequent reflections from other patches received over patch  $i$  ( $R_{LW,i}^m \uparrow (W)$ , Eq. (18)). The first reflection ( $R_{LW,i}^1 \uparrow (W)$ ) is the sum of the reflected fraction of the sky longwave radiation and the reflected fraction of the emitted radiation from all other patches that is incident on patch  $i$ .

$$R_{LW,i} \uparrow = R_{LW,i}^0 \uparrow + R_{LW,i}^1 \uparrow + \sum_{m=2}^{threshold} (R_{LW,i}^m \uparrow) \quad (15),$$

$$R_{LW,i}^0 \uparrow = \varepsilon_i \sigma T_i^4 A_i \quad (16),$$

$$R_{LW,i}^1 \uparrow = \rho_i R_{LW,sky,i} + \rho_i \sum_{j=1}^{npatch} F_{ji} \varepsilon_j \sigma T_j^4 A_j \quad (17),$$

$$R_{LW,i}^m \uparrow = \rho_i \sum_{j=1}^{npatch} F_{ji} (R_{LW,j}^{m-1} \uparrow) \quad (18).$$

In the above equations,  $T_i (K)$  is the surface temperature of patch  $i$  (to be found),  $\varepsilon_i$  is the emissivity of the patch and it is equal to the surface absorptivity, and  $\rho_i$  is the longwave reflectivity of patch  $i$ , assuming the transmissivity of the patch is zero.

### 2.2.3 View Factor

The view factor ( $F_{ij}$ ) of patch  $i$  represents the fraction of radiation leaving the patch surface and reaching another patch  $j$ . This factor depends on the visibility of each pair of patches ( $i, j$ ) with respect to each other, their sizes, distance, and relative orientation. For a pair of patches ( $i, j$ ), the dot product between the outward normal vector of each patch ( $\mathbf{n}_i$  or  $\mathbf{n}_j$ ) and the vector joining centroids of the two patches ( $\mathbf{c}_j \mathbf{c}_i$  or  $\mathbf{c}_i \mathbf{c}_j$ ), i.e.,  $\mathbf{n}_j \cdot \mathbf{c}_j \mathbf{c}_i$  and  $\mathbf{n}_i \cdot \mathbf{c}_i \mathbf{c}_j$ , determines the

visibility of each of the patches with respect to each other. If these dot products are positive, the pair of patches can see each other.

The most commonly used methods to calculate view factors between surfaces are the Monte Carlo method (e.g., in Hoff & Janni, 1989; Howell, 1998; Mirhosseini & Saboonchi, 2011) and the contour integral method (e.g., in Sparrow, 1963; Rao & Sastri, 1996; Mazumder & Ravishankar, 2012). The Monte Carlo method computes view factors as the ratio of the rays incident on a surface patch to the total rays emitted from the other surface based on the radiative emission from that surface. However, since it requires several ray-tracing calculations, it is computationally expensive for 3D surface geometries with high-resolution meshes. Thus, in this work, we employ a contour integral method using vector parametric representation as proposed in Mazumder & Ravishankar (2012). The details of the model are briefly presented in Appendix A.

#### 2.2.4 Shadow Model

The presence of any obstruction between the sun and any triangular patch  $i$  is determined using a ray-tracing method. An obstruction creates a shadow region for patch  $i$ , which is estimated by assessing a direct line of sight between the sun and the patch and locating the intersection of this line and the plane of potential obstructing patches ( $j$ ). This direct line of sight is represented using a 3D equation of a line in vector format, which is calculated using the position vector of the centroid of patch  $i$  ( $\mathbf{c}_i$ ) and the solar unit vector ( $\mathbf{r}_{unit}$ ). Here, the position vector defines the position of any point with respect to a fixed origin (0,0,0). Thus, any point on this line can be found using the centroid of patch  $i$ , which lies on the line and a multiple of the unit vector  $\mathbf{r}_{unit}$  that is parallel to this line as shown below:

$$\mathbf{x} = \mathbf{c}_i + l_p \mathbf{r}_{unit} \quad (19a),$$

$$(x - c_{ix}) = l_p r_{unit,x}; (y - c_{iy}) = l_p r_{unit,y}; (z - c_{iz}) = l_p r_{unit,z} \quad (19b).$$

In Eq. (19),  $c_{ix}$ ,  $c_{iy}$ ,  $c_{iz}$  are the  $x$ ,  $y$ ,  $z$  components of the position vector  $\mathbf{c}_i$ ,  $r_{unit,x}$ ,  $r_{unit,y}$ ,  $r_{unit,z}$  are the  $x$ ,  $y$ ,  $z$  components of the solar unit vector, and  $l_p$  is the parameter describing any point on the line. To estimate whether there is any obstruction over this direct line of sight between patch  $i$  and the sun, the 3D equation of each plane containing other patches ( $j$ ) is found using:

$$(\mathbf{x} - \mathbf{c}_j) \cdot \mathbf{n}_j = 0 \quad (20).$$



Equation (20) describes the vector equation for a plane with a given position vector and a normal. Here,  $\mathbf{n}_j$  is the outward unit normal of patch  $j$  and  $\mathbf{c}_j$  is the position vector of the centroid of patch  $j$ . Subsequently, the position vector of the intersection point ( $\mathbf{c}_{inter}$ ) between the plane through patch  $j$  and the direct line of sight between patch  $i$  and the sun is determined. This intersection point lies on both the plane containing patch  $j$  (Eq. (20)) and the direct line of sight (Eq. (19a)). Thus, the two equations (Eq. (19a) and Eq. (20)) are solved simultaneously and the parameter  $l_p$  is evaluated to find the position vector of the intersection point ( $\mathbf{c}_{inter}$ ):

$$l_p = -\mathbf{n}_j \cdot (\mathbf{c}_i - \mathbf{c}_j) / (\mathbf{n}_j \cdot \mathbf{r}_{unit}) \quad (21),$$

$$\mathbf{c}_{inter} = \mathbf{c}_i + l_p \mathbf{r}_{unit} \quad (22).$$

If this intersection point falls within the triangular patch  $j$ , and the angle ( $\theta$ ) between the normal of patch  $i$  ( $\mathbf{n}_i$ ) and the direct line of sight is between 0 and 90 degrees, then patch  $i$  is deemed to be shaded. Figure 2 shows the diagrammatic representation and the flow chart of the shadow model.

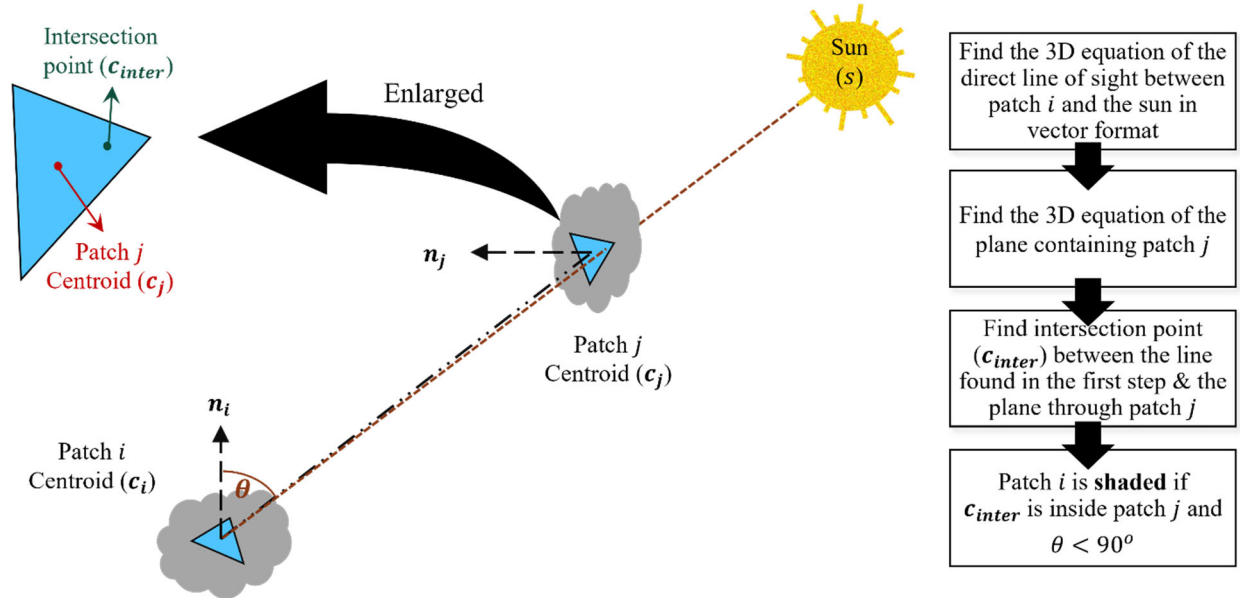


Figure 2: Diagrammatic representation and flow chart of the shadow model, showing patch  $i$  to be shaded due to obstruction by patch  $j$ .

### 2.3 Smoldering Heat Release Rate

If the object under consideration is a smoldering object, the effects of the smoldering heat on the object's temperature are accounted for by considering the smoldering heat release rate ( $Q_{F,i}$  (W)) in the energy budget equation (Eq. (1)).  $Q_{F,i}$  is determined over each patch according to the

heat release rates of the patch material. The smoldering heat release rate is determined based on the  $t^2$ -fire growth model of Kim & Lilley (2000) described in the following equations:

$$\begin{aligned}
 Q_{F,i} &= 0 & 0 \leq t \leq t_o \\
 Q_{F,i} &= \gamma_g(t - t_o)^2 & t_o \leq t \leq t_{lo} \\
 Q_{F,i} &= \gamma_g(t_{lo} - t_o)^2 & t_{lo} \leq t \leq t_d \\
 Q_{F,i} &= \gamma_d(t_{end} - t)^2 & t_d \leq t \leq t_{end} \\
 Q_{F,i} &= 0 & t_{end} \leq t \leq \infty
 \end{aligned} \quad (23).$$

In these equations,  $Q_{F,i}$  (W) is defined for a time period over which a material reaches an ignition point, remains smoldering, and decays to an extinguishing point. In the above equations,  $\gamma_g$  ( $W s^{-2}$ ) is the fire growth coefficient,  $\gamma_d$  ( $W s^{-2}$ ) is the fire decay coefficient,  $t_o$  (s) is the time to the onset of ignition,  $t_{lo}$  (s) is the fire level-off time,  $t_d$  (s) is the time at which  $Q_{F,i}$  decay begins,  $t_{end}$  (s) is the time at which  $Q_{F,i}$  equals 0 (the schematic trend of  $Q_{F,i}$  is shown in Fig. 3). Each of these parameters for a variety of materials is provided in Kim & Lilley (2000).

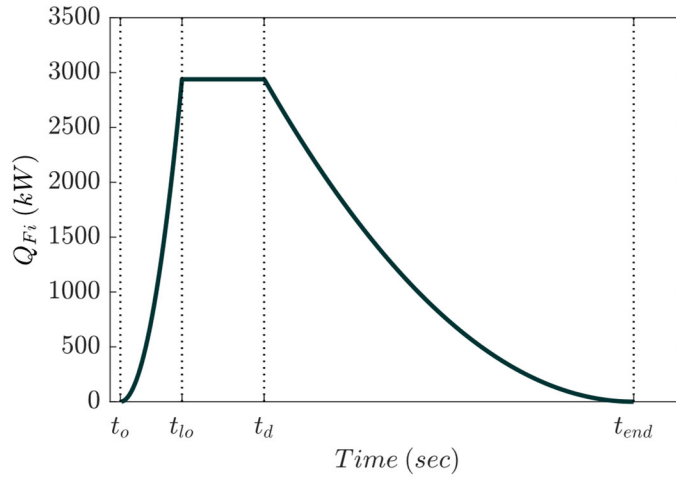


Figure 3: A schematic trend of smoldering heat release rate versus time for a  $t^2$  fire characterization.

## 2.4 Convective Heat Exchange Rate

The rate of convective heat exchanges at each patch is a combination of sensible ( $Q_{H,i}$  (W)) and latent ( $Q_{E,i}$  (W)) heat exchange rates. The cooling effects of the latent heat on the patch surface temperature in the energy balance equation are modeled using a simplified method by employing the Bowen ratio ( $\beta = Q_{H,i}/Q_{E,i}$ ), a prescribed value representing the ratio between the sensible

and latent heat. The sensible convective heat exchange occurring at the patch surface is computed based on:

$$Q_{H,i} = h_i (T_i - T_{air}) A_i \quad (24),$$

in which  $T_{air}$  (K) is the ambient air temperature,  $T_i$  (K) is the surface temperature of patch  $i$  (to be found), and  $h_i$  ( $\text{W m}^{-2} \text{K}^{-1}$ ) is the sensible heat transfer coefficient of the patch.  $h_i$  is approximated either (a) using the bulk (effective) wind speed and air temperature values at the object location, or (b) from the velocity and air temperature local to each individual patch of the object. The former is applied when only bulk values of the ambient wind and air temperature are available, and the latter is applied when high-resolution flow and air temperature data are available, for example, from a computational fluid dynamics (CFD) simulation. For method (a), the effective wind speed and air temperature data at the object location are computed from the reference values obtained from the local weather data files. The reference wind and temperature information in weather files are provided at 10 m and 2 m heights, respectively. Therefore, they are adjusted for the height of each patch according to the log law. The convective heat transfer coefficient ( $h_i$ ) is then estimated using one of the five methods (Nusselt Jurgess, McAdams, the Simple Combined method, TARP, and DOE-2 formulation) included in the model. The details of these methods are provided in Appendix C. In method (b), the same procedure is used for calculating  $h_i$  at each patch surface but with velocities and air temperatures local to each patch.

## 2.5 Conductive Heat Exchange Rate

To capture the evolution of temperature within the object body, 1D conduction within the multi-layer materials of each patch's substrate is considered. Two methods are embedded in the model for the calculation of conduction: a finite difference method (FDM) that uses the Crank-Nicholson time-stepping scheme and an analytical-based Z-transform method that uses the Conduction Transfer Functions (CTFs). The Z-transform method is based on a response factor approach (Stephenson & Mitalas 1967) in which the heat flux at the surface of a material element is related to an infinite series of temperature histories at both the inner and outer extremes of the material layers. The basic form of this approach is:

$$q''(t) = \sum_{cc=0}^{\infty} (XX_{cc} T_{surface}^{t-cc\Delta t} + YY_{cc} T_{in}^{t-cc\Delta t}) \quad (25),$$

where  $q''(t)$  ( $\text{W m}^{-2}$ ) is the heat flux at the surface of an element at the current time  $t$  (s),  $XX$  ( $\text{W m}^{-2} \text{K}^{-1}$ ) and  $YY$  ( $\text{W m}^{-2} \text{K}^{-1}$ ) are response factors,  $T$  (K) is the temperature with subscripts *surface* and *in* indicating the outer and inner extremities of the material layer,  $\Delta t$  (s) is the time step size, and  $cc$  is the number of time steps prior to the current time. Due to the infinite number of response factors required for an exact solution of Eq. (25), Stephenson & Mitalas (1971) further improved the approach by applying the Z-transform theory to the transient heat conduction equation. The improved method forms a conduction transfer solution that reduces the infinite series of response factors by introducing flux history coefficients. This method is computationally efficient and therefore, saves time and computational memory (Stephenson & Mitalas 1971). The conduction transfer solution uses constant CTFs to relate the heat flux at the surface to the current and previous temperatures at the interior and exterior extremities, and the previous heat fluxes. The basic form of the improved Z-Transform equation is:

$$\begin{aligned}
q''_{surface,t} = & X_0 T_{surface}^t - Y_0 T_{in}^t + \sum_{cc=1}^{nx} X_{cc} T_{surface}^{t-cc\Delta t} - \sum_{cc=1}^{ny} Y_{cc} T_{in}^{t-cc\Delta t} \\
& + \sum_{cc=1}^{nq} \Phi_{cc} q''_{surface,t-cc\Delta t}
\end{aligned} \tag{26},$$

where,  $q''_{surface,t}$  ( $\text{W m}^{-2}$ ) is the surface conductive heat flux at the current time step  $t$  (s). In this equation,  $X$  ( $\text{W m}^{-2} \text{K}^{-1}$ ),  $Y$  ( $\text{W m}^{-2} \text{K}^{-1}$ ), and  $\Phi$  are the constant CTFs for the element's exterior extreme, interior extreme, and surface flux with subscript 0 indicating the current time step.  $q''_{surface,t-cc\Delta t}$  ( $\text{W m}^{-2}$ ) is the heat flux at the element's outside surface at  $cc$  time steps prior to the current time  $t$  (s), and  $nx$ ,  $ny$ , and  $nq$  are the maximum number of CTF terms. The CTF coefficients are determined only once for each construction type and are computed using a state-space method (Ceylan & Mayres 1980; Seem 1987), where the maximum number of CTF terms is limited to 19.  $q''_{surface,t}$  is then used to find the rate of conductive heat ( $Q_{G,i}$  (W)) for each patch in Eq. (1) using the patch surface area ( $A_i$  ( $\text{m}^2$ )).

As Eq. (26) shows, the Z-transform method provides a single, linear equation with pre-calculated CTF constants and does not require information from within the material. Therefore, it provides an efficient method for the calculation of conduction and requires a limited space for data

storage. As a result, this method significantly reduces the overall computational time in comparison with the FDM.

The FDM is used when information on the temperature evolution within the object material is needed. In the FDM, the conduction into the multiple substrate layers of each surface patch is simulated according to:

$$T_L^{t+1} - T_L^t = \frac{\Delta t}{\rho_L C_L \Delta x_L} \left[ \frac{1}{2} (G_{L-1,L}^{t+1} - G_{L,L+1}^{t+1}) + \frac{1}{2} (G_{L-1,L}^t - G_{L,L+1}^t) \right] \quad (27a),$$

$$G_{L-1,L}^t = k_{L-1,L} \frac{(T_{L-1}^t - T_L^t)}{\frac{1}{2} (\Delta x_{L-1} + \Delta x_L)} \quad (27b).$$

Here,  $T_L$  (K),  $\rho_L$  ( $\text{kg m}^{-3}$ ),  $\Delta x_L$  (m), and  $C_L$  ( $\text{J kg}^{-1} \text{K}^{-1}$ ) are, respectively, the temperature, density, thickness, and specific heat capacity of material layer  $L$ .  $G_{L-1,L}^t$  ( $\text{W m}^{-2}$ ) is the conductive heat flux between layers  $L - 1$  and  $L$  at timestep  $t$ , where  $k_{L-1,L}$  ( $\text{W m}^{-1} \text{K}^{-1}$ ) is the conductivity between layers  $L - 1$  and  $L$ .

Externally, conduction, in both methods, is bounded by the patch surface temperature. For the FDM, following Krayenhoff & Voogt (2007), a conduction flux density condition is employed to find the temperature of the first layer under the patch ( $T_1$ ) based on:

$$T_1^{t+1} - T_1^t = \frac{\Delta t}{\rho_1 C_1 \Delta x_1} \left[ G_{surface,1}^{t+1} - \frac{1}{2} G_{1,2}^{t+1} - \frac{1}{2} G_{1,2}^{t+1} \right] \quad (28).$$

Temperatures of all material layers ( $T_L$  (K),  $L$  from 1 to the deepest layer) are solved at each time step for each patch. Then, the patch surface temperature ( $T_{surface}^{t+1}$ ) at the next time step is solved using the energy balance equation (Eq. (1)), where the conduction term for the FDM is:

$$Q_{G,i} = -k_1 A_i \frac{(T_{surface}^{t+1} - T_1^t)}{0.5 \Delta x_1} \quad (29).$$

Internally, conduction, in both methods, is bounded by the internal body temperature. The inner extreme of the patch substrate is bounded either by an internal object temperature for a non-ground patch (defined as patches that are not attached to the ground level) or by a deep underground temperature for a ground-level patch. The internal object temperature can be prescribed or can be estimated based on the average surface temperature of the object over some previous timesteps. Following Hillel (1982), the deep underground temperature,  $T_{deep}$  (K), at all depths is assumed to vary sinusoidally around an average value, where the amplitude of the fluctuation dampens with the depth below the ground surface based on the thermal properties of the underground material.

This estimation reflects the periodic diurnal and seasonal interactions of the soil and atmosphere.  $T_{deep}$  at time  $t$  (s) and depth  $z$  (m) is thus estimated based on:

$$T_{deep}(z, t) = T_{avg} + A_o e^{-\frac{z}{D}} \sin\left(\frac{2\pi t}{P} - \frac{z}{D}\right) \quad (30),$$

where,  $T_{avg}$  (K) is the average surface temperature over a time period  $P$  (s),  $A_o$  (K) is the amplitude of the surface temperature over the same period,  $D = \sqrt{kP/(\rho C_p \pi)}$  (m) is the thermal dampening depth related to the thermal properties of the ground and temperature fluctuations.  $k$  ( $\text{W m}^{-1} \text{K}^{-1}$ ),  $C_p$  ( $\text{J kg}^{-1} \text{K}^{-1}$ ), and  $\rho$  ( $\text{kg m}^{-3}$ ) are the conductivity, specific heat capacity, and density of the soil/ground. The maximum depth for the calculation of  $T_{deep}$  (K) is limited to  $z = 3D$  since at this depth the soil temperature amplitude is small (5% or less) compared to the amplitude of the surface temperature ( $A_o$ ) (Hillel, 1982).

In general, FDM does not have a geometric or temporal limitation, but it requires storage for each material layer and thus, is computationally costly in comparison to the Z-transform method. On the other hand, the Z-transform method is known to cause stability problems for very short time steps and for when thick materials are under investigation. For this reason, both conduction methods have been implemented in the model, and depending on the complexity of the object, time steps, and material layer thicknesses an appropriate method is used.

### 3. Full Model Validation

While the accurate formulation of each sub-model was verified and the performance of each was validated individually against analytical solutions or measured data, the holistic performance of TERSO was tested against measurements from three experiments reported in the literature. For the sake of brevity, only the full model tests are presented here. In the first test, the model prediction was evaluated against field data, as well as data from a 3D urban energy balance model TUF-3D (Krayenhoff & Voogt 2007) for a light industrial site in Vancouver, Canada under diurnally varying environmental conditions. In the second and third tests, the model results for smoldering objects were compared against laboratory experiments with different smoldering conditions.

#### 3.1 Validation of the non-smoldering object model for diurnally variable environmental conditions

The field experiment site in Vancouver consists of one- to three-story buildings with a rectangular footprint, flat roofs, and no vegetation. The measurements were conducted on August 15, 1992, during the presence of well-defined sunlit and shaded patterns over the structures. Walls and street surface temperatures were measured using truck-mounted remote thermal sensors. While, for the roof, airborne thermal remotely sensed radiative surface temperatures were acquired. Further details about the site and measurements are available in Krayenhoff & Voogt (2007) and Voogt & Grimmond (2000). A 3-by-3 array of uniformly spaced buildings was configured for this validation study using the geometrical ratios as in Krayenhoff & Voogt (2007) and the results were analyzed for the central building unit to be compared with those of TUF-3D. The building material's thermal properties (obtained from Krayenhoff & Voogt 2007) are shown in Table 1. In the absence of weather data for the date of the measurements (e.g., air temperature, wind speed, radiation), the required weather condition information was extracted from the available TMY files. Using this weather data, the model was run over a period of four days from August 12 to August 15, with the first three days being considered as the spin-up period and the results from the last day were used for the comparisons. Here, the DOE-2 convection model was used for the vertical walls and the Simple Combined method was employed for the horizontal surfaces of the roofs and streets.

**Table 1** Wall, roof, and street material layers from the outer to the inner layer (based on Table 2 of Krayenhoff & Voogt, 2007)

Material layers	Thickness (m)	Conductivity ( $\text{W m}^{-1} \text{K}^{-1}$ )	Density ( $\text{kg m}^{-3}$ )	Specific heat ( $\text{kJ kg}^{-1} \text{K}^{-1}$ )	Albedo	Emissivity
<b>Walls</b> ( $T_{\text{initial}}=19^{\circ}\text{C}$ )						
Layer 1 (outer)	0.03	1.51	2400	0.88	0.5	0.9
Layer 2	0.07	0.67	1600	0.625	-	-
Layer 3	0.07	0.67	1600	0.625	-	-
Layer 4 (inner)	0.03	1.51	2400	0.88	0.5	0.9
<b>Roof</b> ( $T_{\text{initial}}=12^{\circ}\text{C}$ )						
Layer 1 (outer)	0.015	1.4	2000	0.88	0.12	0.92
Layer 2	0.015	1.4	2000	0.88	-	-
Layer 3 (Insulation)	0.01	0.03	40	1.0	-	-
Layer 4 (inner)	0.03	1.51	2400	0.92	-	-
<b>Street</b> ( $T_{\text{initial}}=20^{\circ}\text{C}$ )						
Layer 1 (outer)	0.05	0.82	2110	0.82	0.08	0.95
Layer 2	0.2	2.1	2400	0.83	-	-
Layer 3	0.1	0.4	1300	1.08	-	-

Layer 4 (inner)	0.1	0.4	1300	1.08	-	-
-----------------	-----	-----	------	------	---	---

Figure 4 compares the average surface temperatures of the north (N), south (S), east (E), and west (W) facing walls from TERSO against the measured data and the TUF-3D modeled data. The results indicate that the diurnal changes in the wall surface temperatures throughout the day are well captured by TERSO. This is further verified in Table 2, which shows the root mean square errors (RMSE) between the simulated and observed data. For comparison, the table also includes the RMSE for the TUF-3D model (obtained from Krayenhoff & Voogt 2007). The slight differences between the model output and observations are potentially related to the weather data input into the model, which was not provided in the reference literature and, therefore, obtained from the available TMY weather data files.

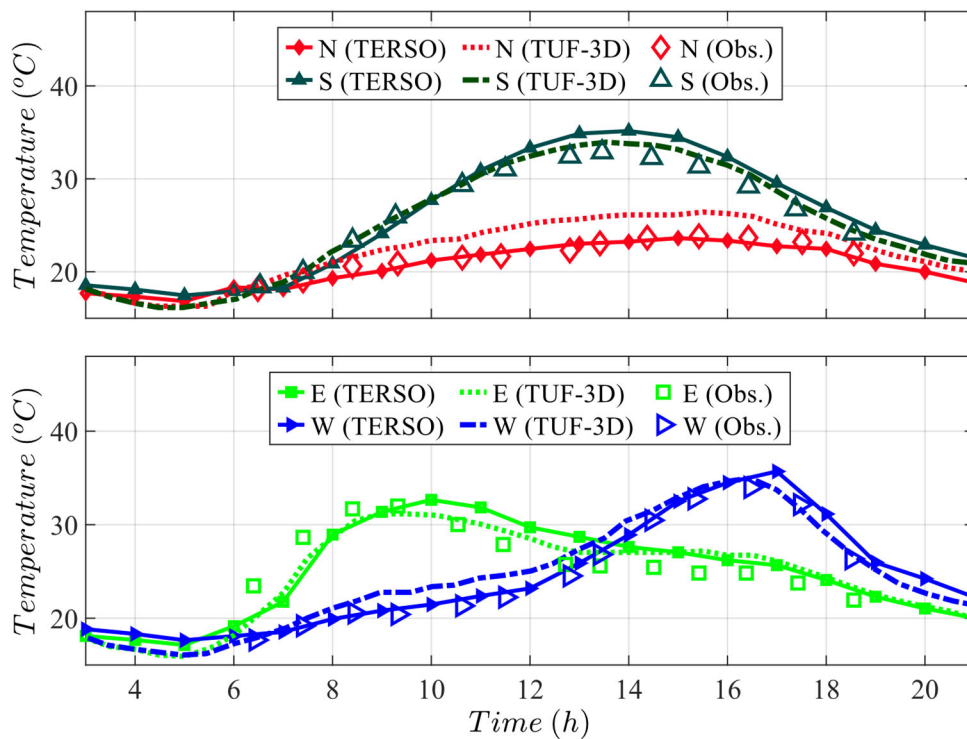


Figure 4: Comparison of TERSO outputs against measured data (Obs.) and the simulated results of TUF-3D for facet-average surface temperatures of the north (N), south (S), east (E), and west (W) facing walls throughout the day for Aug 15, 1992, in the Vancouver Light Industrial site.

**Table 2** Root Mean Square Errors (RMSE) between simulated surface temperatures and observations for the Vancouver Light Industrial site. RMSE of the TUF-3D model is shown for comparison.



<b>Material layers</b>	<b>N - wall</b>	<b>S - wall</b>	<b>E - wall</b>	<b>W - wall</b>
TERSO	0.5	1.5	2.1	0.9
TUF-3D	2.2	0.8	1.9	1.6

Figure 5 compares the diurnal changes between the observed data and TERSO and TUF-3D modeled data for the average roof and street surface temperatures. It can be seen that the simulated results of TERSO for the roof surface temperatures compare well with the field observations and show a better prediction compared to that of TUF-3D. A maximum difference of 3.24°C compared to 12.97°C of the TUF-3D model is seen between the field observations and TERSO. The underperformance of TUF-3D, in this case, was related to the uncertainty in the surface roughness length (that is used in the Monin–Obukhov similarity theory (MOST) formulation of the convection model for horizontal surfaces), insulation layer thickness, and radiative parameters (Krayenhoff & Voogt, 2007). In the current model, the same input for the insulation layer thickness is used. However, the surface roughness length is not employed in TERSO (due to the use of a different convection model (i.e., the Simple Combined method) for horizontal surfaces than the MOST method) and the radiative parameters and the air temperature information are obtained from TMY files rather than from helicopter reading (due to their absence). The simulated street temperatures compare well with the observations in the morning, however, they are underestimated after midday with a maximum difference of 10.99°C compared to 5.34°C of the TUF-3D model. This difference is also potentially related to the use of different convection models for the horizontal surfaces and different sources for the local weather data in the two models.

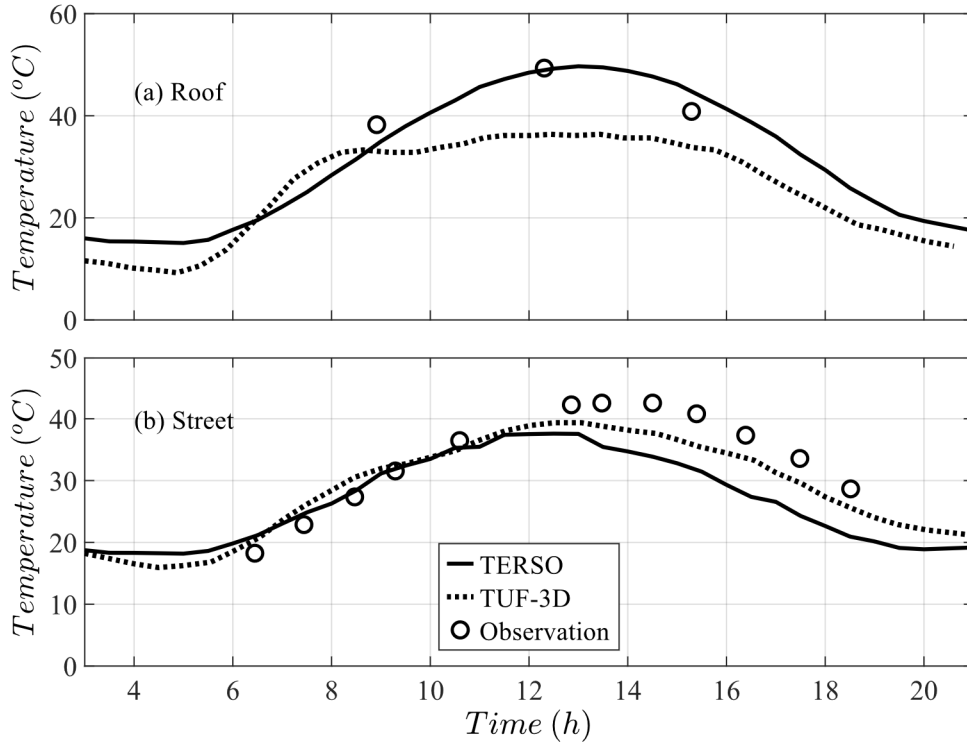


Figure 5: Comparison of TERSO outputs against measured data (Obs.) and simulation results of TUF-3D for facet-average surface temperatures of the (a) roof and (b) street throughout the day of Aug 15, 1992, in the Vancouver Light Industrial site.

### 3.2 Validation of the smoldering object model

To test the accuracy of temperature evolution predicted by the model for smoldering objects, the model results were compared against the measured data of two different piloted ignition experiments of wildland fuel beds (Mindykowski et al. 2011; Rivera et al. 2020). The fuel beds in both of these controlled experiments were made of combustible materials that were heated by either smoldering firebrands (Rivera et al. 2020) or infrared heaters (Mindykowski et al. 2011). In the experimental setup by Mindykowski et al. (2011), dead and dried Maritime Pine needles were used and placed in a cylindrical steel basket holder with a diameter of 0.126 m and a height of 0.03 m. Longer needles were cut using scissors and all the needles were randomly placed by hand within the basket to reach a desired volume fraction ( $V_{frac}$ ) in four different experiments with different incident heat fluxes. The heat was generated using infrared heaters that were located at a distance of 0.073 m above the fuel basket. The imposed heat ranged from  $12.5 \text{ kW m}^{-2}$  to  $30 \text{ kW m}^{-2}$  in increments of  $2.5 \text{ kW m}^{-2}$  and the time to ignition was recorded at the visual appearance of flaming combustion for each incident heat flux. The time of flaming was also verified using a recorded

video. More information on the experimental setup can be found in Mindykowski et al. (2011). To numerically emulate this experiment, a similar setup was considered in the computational model. However, since replication of the random setup of the fuel elements is not practical, a solid material with equivalent effective conductivity ( $k_{eq}$ ) was considered in TERSO. The equivalent conductivity was determined based on the reported volume fraction of needles, and was calculated using the following equation (Mindykowski et al. 2011):

$$k_{eq} = (1 - V_{frac}) k_{air} + V_{frac} k_m \quad (31).$$

In this equation,  $k_{air}$  and  $k_m$  are the conductivity of the air and medium (needles) under consideration.  $k_m$  ( $= 0.12 \text{ W m}^{-1} \text{ K}^{-1}$ ; Baranovskiy & Malinin 2020) was set to the conductivity of the pinewood material as the conductivity of the Maritime Pine needles was not provided by Mindykowski et al. (2011). The other relevant material and thermal properties of the Maritime Pine needle fuel bed used in the simulations are based on Mindykowski et al. (2011) and listed in Table 3. The experiments were done indoors, therefore no solar radiation was considered in the numerical model. For the convection model, due to the absence of relevant parameter information for calculating the convection coefficient, this coefficient was set to  $15 \text{ W m}^{-2} \text{ K}^{-1}$  (based on the theoretical solution presented in Rivera et al. (2020)) and the ambient air temperature was set to a typical room temperature of  $25^\circ\text{C}$ .

**Table 3** Thermal and material properties of wildland fuel beds for Maritime Pine needles (Mindykowski et al. 2011) and Monterey Pine needles (Rivera et al. 2020)

Fuel Type	Volume fraction	Density ( $\text{kg m}^{-3}$ )	Heat Capacity ( $\text{J kg}^{-1}\text{K}^{-1}$ )	Ignition Temp. (K)	Emissivity	Convection Coefficient ( $\text{W m}^{-2}\text{K}^{-1}$ )	Equivalent Density ( $\text{kg m}^{-3}$ )	Equivalent Conductivity ( $\text{W m}^{-1}\text{K}^{-1}$ )	Material thickness (m)
Maritime Pine needles	0.08	630	1470	400	0.8646	15	51.53	0.3168	0.036
Monterey Pine needles	0.09	615.3	1470	549	0.8646	15	56.49	0.3264	0.045

Figure 6 compares the time taken for the average temperature of the entire fuel layer in the sample holder to reach the ignition temperature ( $t_{ignition}$ ) between the simulation and experiment for the provided range of incident heat fluxes. The figure shows a good agreement between the model and experimental data for high incident heat fluxes. However, ignition times for the lower

range of heat fluxes are underestimated. This underestimation is potentially related to the comparison of the average temperatures of the entire material layer, which is not completely accurate for the lower incident heat fluxes since the needles closer to the heat source are likely to reach the ignition temperatures sooner. Other sources of differences could be related to the differences in the experimental and numerical setups: In the experiments, the pine needles were distributed randomly, while the numerical setup employs equivalent thermal and material properties of the combined setup that includes the needles and the air gaps. Equivalent properties were used in these simulations since the dimensions of each needle in the fuel layer are unknown, which together with the random distribution makes it impractical to accurately replicate the exact experimental setup.

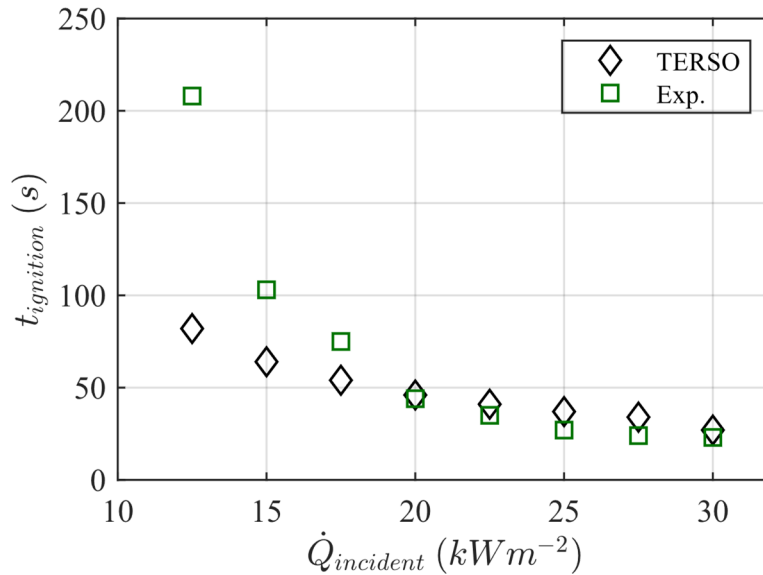


Figure 6: Comparison of the ignition time as a function of incident heat flux between the TERSO results and the experimental data from Mindykowski et al. (2011) for a Maritime Pine needle fuel layer

The second validation study for the smoldering model was conducted using the experimental data of Rivera et al. (2020) in which a set of ignition experiments were carried out on an idealized firebrand-ignition test bench-scale apparatus with dead and dried Monterey Pine needles. The experimental setup consisted of a cylindrical-shaped sample holder with a radius of 0.065 m and a height of 0.046 m, with an axisymmetric void at the center with a radius of 0.02m. A small cylindrical-shaped heater element (representing an idealized firebrand) was placed vertically at the center of the void to provide varying incident heat flux to the fuel layer. Similar to the experiments by Mindykowski et al. (2011), the pine needles were randomly placed inside the sample holder by

hand to achieve a desired volume fraction for the fuel layer. The time to ignition of the fuel layer in this setup was recorded at the initial appearance of a flame. A similar setup was used in TERSO to evaluate the numerical model performance. As in the experiments, the inner surface of the hollow cylinder was exposed to various heat fluxes ranging from  $6.6 \text{ kW m}^{-2}$  to  $24.6 \text{ kW m}^{-2}$ . The equivalent density, equivalent conductivity, and thermal and material properties of the fuel layer are presented in Table 3 based on Rivera et al. (2020). Similar to the validation study against the Mindykowski et al. (2011) case, the convection coefficient was fixed at  $15 \text{ W m}^{-2} \text{ K}^{-1}$  (Rivera et al. 2020), the external air temperature was set at  $25^\circ\text{C}$ , and the FDM was employed for the calculation of conduction.

Figure 7 compares the numerical results of TERSO against measured data for  $t_{\text{ignition}}$  (i.e., the time taken for the average temperature of the fuel layer to reach the ignition temperature) for various incident heat fluxes. The results show a good performance of the model, except for the lowest incident heat flux, where the highest experimental error was reported. The experiments at lower heat fluxes tend to have higher errors as the needles are likely to be consumed before ignition is attained (Rivera et al. 2020). The lower ignition time prediction by the model is likely to be related to the comparison of the average material layer temperature compared against that of the experiment. Analogous to the previous validation study, the other minor differences between the model and the experiment is likely to be related to the use of equivalent material properties since the exact random setup of the fuel needles within the sample holder is not achievable.

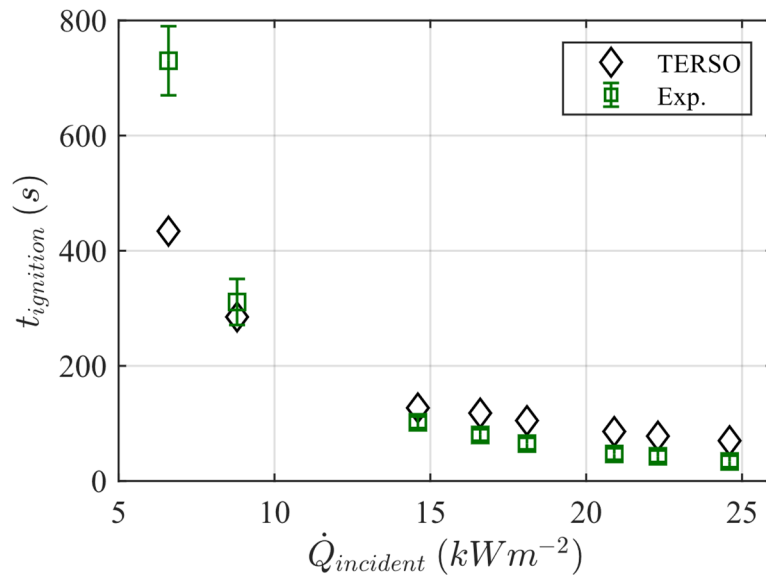


Figure 7: Comparison of ignition time as a function of incident heat flux between the model and experiments from Rivera et al. (2020) on the Monterey Pine needle fuel layer.

## 4. Conclusions

A new surface energy balance model, Temperature Evolution of Random-shaped Smoldering Objects (TERSO), is developed to predict the spatiotemporal surface and body temperature evolution of smoldering and non-smoldering 3D objects under variable environmental conditions. The objects under investigation can be of any random shape and made of multiple materials and material layers. The open-environment weather and solar radiation data is obtained from available typical meteorological year (TMY) weather data files, which are available for each geographical location, and the information on the smoldering heat release rate for each material is obtained from Kim & Lilley (2000). The environmental attributes and thermal and material properties of each sub-surface (or patch) in the model are local to each patch, and a thorough treatment of radiation exchanges consisting of multiple shortwave and longwave reflections is considered. A ray-tracing shadow sub-model has been developed and incorporated into the model to precisely represent the spatiotemporal variations of the shadow distributions in case any exists. Following tests of the sub-models, the performance of the whole model for non-smoldering objects under diurnally variable environmental conditions has been validated against field measurements (Voogt & Grimmond, 2000) and modeled surface temperatures from an urban energy balance model (Krayenhoff & Voogt 2007), displaying close agreements with both. The model performance has also been evaluated for smoldering objects using the results of two controlled experiments (Mindykowski et al. 2011; Rivera et al. 2020). The results of the validation studies indicated the ability of the model in accurate predictions of temperature evolution of smoldering and non-smoldering objects under different conditions. The discrete, high spatiotemporal resolution surface temperature information of TERSO can also be used to provide unsteady thermal boundary conditions for computational fluid dynamics simulations when coupled physics is under investigation. TERSO can be improved in different aspects, for example, in its treatment of the latent heat flux to include a detailed moisture model. It can also be enhanced to include material layer transmissivity in the radiation computations for each patch to consider porous materials.

## **Acknowledgment**

This work is supported by funding from the Department of Defense Strategic Environmental Research and Development Program (SERDP) RC20-1298.

## Appendix A View Factor Model

The view factor model used in this study employs the contour integral (Eq. (33); Sparrow 1963) representation of the well-known form (Eq. (32); Bergman et al. 2011) of the view factor ( $F_{QP}$ ) between two patches  $Q$  and  $P$ :

$$F_{QP} = \frac{1}{A_Q} \int \int \frac{\cos\theta_Q \cos\theta_P}{\pi R^2} dA_Q dA_P \quad (32),$$

$$F_{QP} = \frac{1}{2\pi A_Q} \oint \oint \ln S \, \mathbf{ds}_Q \, \mathbf{ds}_P \quad (33),$$

where  $\theta_Q$  is the angle between the outward normal of the patch  $Q$  and the line joining patches  $P$  and  $Q$ ,  $\theta_P$  is the angle between the outward normal of the patch  $P$  and the line joining patches  $P$  and  $Q$ ,  $R$  (m) is the distance between the two patches.  $A_Q$  ( $\text{m}^2$ ) and  $A_P$  ( $\text{m}^2$ ) are the areas of patches  $P$  and  $Q$ , respectively, and  $S$  is the distance between two differential line vectors ( $\mathbf{ds}_Q$  and  $\mathbf{ds}_P$ ) as shown in Fig. 8. This contour formula is then transformed into a vector parametric representation (Mazumder & Ravishankar 2012):

$$\begin{aligned} F_{QP} = \frac{1}{4\pi A_Q} \sum_{n=1}^N \sum_{m=1}^M \int_0^1 \int_0^1 & \ln \left( \lambda_Q^2 |\mathbf{q}_{m,m+1}|^2 + \lambda_P^2 |\mathbf{p}_{n,n+1}|^2 + |\mathbf{Q}_m \mathbf{P}_n|^2 \right. \\ & - 2\lambda_Q \mathbf{Q}_m \mathbf{P}_n \cdot \mathbf{q}_{m,m+1} + 2\lambda_P \mathbf{Q}_m \mathbf{P}_n \cdot \mathbf{p}_{n,n+1} \\ & \left. - 2\lambda_Q \lambda_P \mathbf{p}_{n,n+1} \cdot \mathbf{q}_{m,m+1} \right) \mathbf{p}_{n,n+1} \cdot \mathbf{q}_{m,m+1} \, d\lambda_Q \, d\lambda_P \end{aligned} \quad (34).$$

In this equation,  $\mathbf{p}_{n,n+1}$  and  $\mathbf{q}_{m,m+1}$  are vectors on the contours of polygons  $P$  and  $Q$ , respectively, directed from one vertex of the polygon to the other.  $\mathbf{Q}_m \mathbf{P}_n$  is a vector from a vertex on polygon  $Q$  to a vertex on polygon  $P$ .  $0 < \lambda_P < 1$  and  $0 < \lambda_Q < 1$  represent a fraction of the vectors  $\mathbf{p}_{n,n+1}$  and  $\mathbf{q}_{m,m+1}$ . The integral in Eq. (34) is calculated using the 10-point Gauss-Legendre quadrature scheme (Appendix B) (Beyer 1996). If an edge is shared between the polygons, the following relation is used

$$F_{QP\_shared} = |\mathbf{q}_{shared\ edge}|^2 \left( 1.5 - 0.5 \ln \left( |\mathbf{q}_{shared\ edge}|^2 \right) \right) \quad (35),$$

Where,  $|\mathbf{q}_{shared\ edge}|$  is the length of the shared edge. Please refer to Mazumder and Ravishankar (2012) for further details.

The view factor implementation in this model was verified with the cases presented in Mazumder & Ravishankar (2012) and Hoff & Janni (1989) with excellent accuracy.



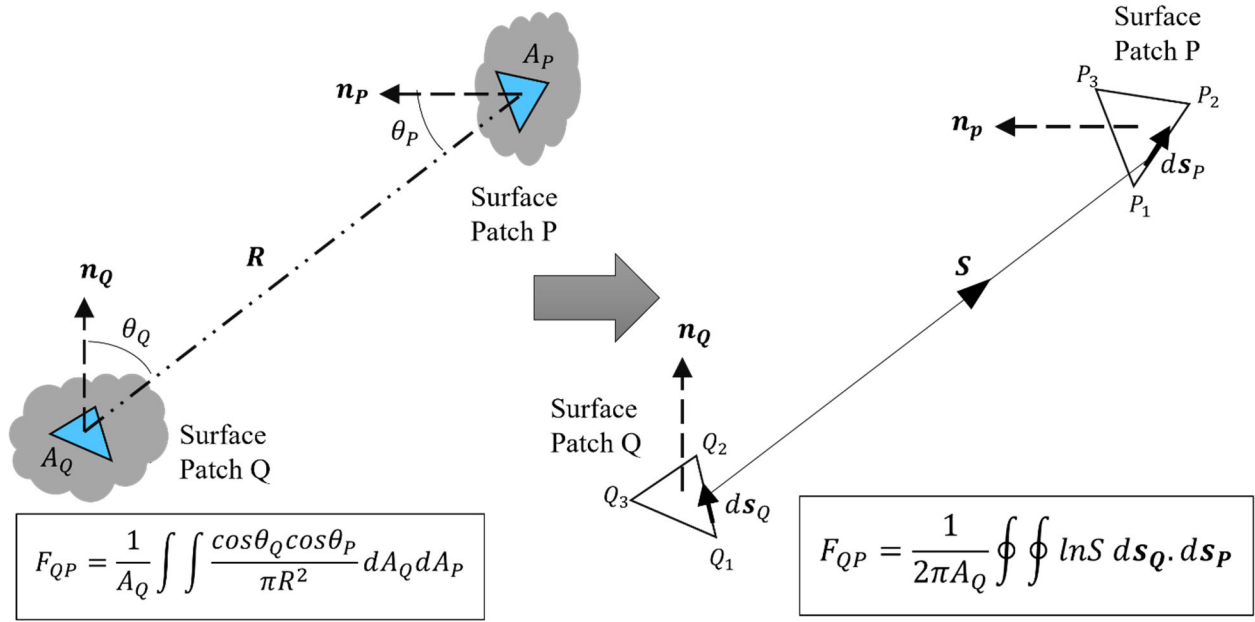


Figure 8: Diagrammatic representation of the conversion of the well-known view factor form to a vector parametric contour integral form for a triangular patch.

## Appendix B Gauss-Legendre Quadrature Scheme

To evaluate the integrals in Eq. (34), the following scheme is used (Beyer 1996):

$$\int_a^b f(x) dx = \sum_{i=1}^{\infty} w_i f(x_i) \approx \sum_{i=1}^n w_i f(x_i) \quad (36).$$

Here,  $f(x)$  is the integral to be evaluated,  $(a, b)$  are the limits of the integration,  $n$  is the number of points used in the scheme,  $w_i$  are the weights or coefficients, and  $x_i$  are the nodes or abscissa. The weights ( $w_i$ ) and nodes ( $x_i$ ) are chosen to achieve maximum accuracy. Here, a 10-point Gaussian quadrature scheme is used ( $n = 10$ ). The weights and nodes used in this scheme are shown in Table 4. This scheme requires the integral limits to be within the range  $(-1, 1)$ , which entails the transformation of the coordinates in the following manner:

$$\begin{aligned} \int_a^b f(x) dx &= \frac{(b-a)}{2} \int_{-1}^1 f\left(\frac{b-a}{2} x_i + \frac{b+a}{2}\right) dx \\ &\approx \frac{(b-a)}{2} \sum_{i=1}^n w_i f\left(\frac{b-a}{2} x_i + \frac{b+a}{2}\right) \end{aligned} \quad (37).$$

**Table 4** The weights ( $w_i$ ) and nodes ( $x_i$ ) used for a 10-point Gaussian quadrature scheme

$i$	weight - $w_i$	abscissa - $x_i$
1	0.295524225	-0.148874339
2	0.295524225	0.148874339
3	0.269266719	-0.433395394
4	0.269266719	0.433395394
5	0.219086363	-0.679409568
6	0.219086363	0.679409568
7	0.149451349	-0.865063367
8	0.149451349	0.865063367
9	0.066671344	-0.973906529
10	0.066671344	0.973906529

## Appendix C Convection Methods

### Nusselt Jurgess

This method constitutes of a large constant that represents the natural convection part of the total convection coefficient. The method can be applied to surfaces/patches with any orientation or roughness. This method takes the following simplified form in the SI units (Nusselt & Jurgess 1922; Palyvos 2008):

$$h = 5.8 + 3.94V_z \quad (38),$$

where  $h$  ( $\text{W m}^{-2} \text{K}^{-1}$ ) is the convection coefficient and  $V_z$  ( $\text{m s}^{-1}$ ) is the local wind velocity, which is adjusted according to the height of the surface patch's centroid.

### McAdams

This method has similar characteristics to the Nusselt Jurgess method. The form of this equation in the SI units is (McAdams 1954; Palyvos 2008):

$$h = 5.7 + 3.8V_z \quad (39).$$

### The Simple Combined Method

This method uses the local wind velocity ( $V_z$  ( $\text{m s}^{-1}$ )) and the surface roughness parameters ( $D$  ( $\text{W m}^{-2} \text{K}^{-1}$ ),  $E$  ( $\text{J m}^{-3} \text{K}^{-1}$ ), and  $F$  ( $\text{J s m}^{-4} \text{K}^{-1}$ )) to calculate the convection coefficient (EnergyPlus 2021):

$$h = D + EV_z + FV_z^2 \quad (40).$$

**Table 5** Roughness coefficients for the Simple Combined Method (ASHRAE 1989)

<b>Roughness Index</b>	<b>D</b> <b>(W m<sup>-2</sup> K<sup>-1</sup>)</b>	<b>E</b> <b>(J m<sup>-3</sup> K<sup>-1</sup>)</b>	<b>F</b> <b>(J s m<sup>-4</sup> K<sup>-1</sup>)</b>
1. Very Rough	11.58	5.894	0.0
2. Rough	12.49	4.065	0.028
3. Medium Rough	10.79	4.192	0.0
4. Medium Smooth	8.23	4.0	-0.057
5. Smooth	10.22	3.1	0.0
6. Very Smooth	8.23	3.33	-0.036

## TARP

Thermal Analysis Research Program (TARP) model is a comprehensive convection model, which combines a correlation from ASHRAE and the flat plate experiments by Sparrow et al. 1979 (Walton 1983). In this model, the convection is split into forced and natural components, where the forced component (Eq. (42)) is based on a correlation by Sparrow et al. 1979:

$$h = h_{natural} + h_{forced} \quad (41),$$

$$h_{forced} = 2.537W_f R_f \left( \frac{PV_z}{A} \right)^{0.5} \quad (42).$$

Here,  $h_{natural}$  (W m<sup>-2</sup> K<sup>-1</sup>) is the natural convection coefficient,  $h_{forced}$  (W m<sup>-2</sup> K<sup>-1</sup>) is the forced convection coefficient, and  $V_z$  (m s<sup>-1</sup>) is the local wind velocity in m s<sup>-1</sup>, which is adjusted according to the height of the surface patch's centroid.  $A$  (m<sup>2</sup>) is the area of the surface,  $W_f$  is equal to 1 for the windward surfaces and 0.5 for the leeward surfaces,  $R_f$  is a surface roughness multiplier, and  $P$  (m) is the perimeter of the surface.

**Table 6** Surface roughness multipliers (Walton 1981)

<b>Roughness Index</b>	<b><math>R_f</math></b>
1. Very Rough	2.17
2. Rough	1.67
3. Medium Rough	1.52
4. Medium Smooth	1.13
5. Smooth	1.11
6. Very Smooth	1.0

The natural component is calculated based on the following: For  $\Delta T = 0$  or vertical surfaces, where  $\Delta T$  is the temperature difference between the surface and air:

$$h_{natural} = 1.31 |\Delta T|^{1/3} \quad (43).$$

For  $\Delta T > 0$  and a downward-facing surface or  $\Delta T < 0$  and an upward-facing surface:

$$h_{natural} = \frac{9.482|\Delta T|^{1/3}}{7.283 - |\cos \epsilon|} \quad (44).$$

For  $\Delta T > 0$  and an upward-facing surface or  $\Delta T < 0$  and a downward-facing surface:

$$h_{natural} = \frac{1.81|\Delta T|^{1/3}}{1.382 + |\cos \epsilon|} \quad (45).$$

Here,  $\epsilon$  is the surface tilt angle between the ground outward normal and the surface outward normal.

### The DOE-2 Method

The DOE-2 convection model is the combination of the MoWiTT and BLAST Detailed models (LBL 1994). The BLAST model is similar to the TARP model with the calculation of the local wind velocity ( $V_z$ ) being the only difference between the two (Mirsadeghi et al. 2013). The MoWiTT algorithm applies to smooth, vertical surfaces and has the following form:

$$h_c = \sqrt{(C_1(\Delta T)^{1/3})^2 + (aV_z^b)^2} \quad (46).$$

Here  $h_c$  ( $\text{W m}^{-2} \text{K}^{-1}$ ) is the convection coefficient for very smooth surfaces,  $a$  and  $b$  are constants, and  $C_1$  is a turbulent natural convection coefficient.

**Table 7** MoWiTT Coefficients (Yazdanian and Klems 1994; Booten et al. 2012)

Wind Direction	$C_1$ ( $\text{W m}^{-2}\text{K}^{-(4/3)}$ )	$a$ ( $\text{W m}^{-2}\text{K} (\text{m s}^{-1})^b$ )	$b$ -
Windward	0.84	3.26	0.89
Leeward	0.84	3.55	0.617

The DOE-2 method employs the following method to calculate the convection coefficient:

$$h = h_{natural} + R_f(h_c - h_{natural}) \quad (47),$$

where,  $R_f$  is the surface roughness multiplier (Table 6) and  $h_{natural}$  is the natural convection coefficient that is calculated from Eq. (43), (44), and (45).

## **Data Availability**

The data that support the findings of this study are available from the corresponding author upon reasonable request.

## References

- Anthenien, R. A., Stephen, D. T., & Fernandez-Pello, A. C. (2006). On the trajectories of embers initially elevated or lofted by small scale ground fire plumes in high winds. *Fire Safety Journal*, 41(5), 349-363.
- Arnfield, A. J. (1990). Canyon geometry, the urban fabric and nocturnal cooling: a simulation approach. *Physical Geography*, 11(3), 220-239.
- Asawa, T., Hoyano, A., & Nakaohkubo, K. (2008). Thermal design tool for outdoor spaces based on heat balance simulation using a 3D-CAD system. *Building and Environment*, 43(12), 2112-2123.
- ASHRAE. 1989. 1989 ASHRAE Handbook – Fundamentals, Atlanta: American Society of Heating, Refrigerating, and Air-Conditioning Engineers, Inc.
- Baek, S. W., Kim, M. Y., & Kim, J. S. (1998). Nonorthogonal finite-volume solutions of radiative heat transfer in a three-dimensional enclosure. *Numerical Heat Transfer, Part B*, 34(4), 419-437.
- Baranovskiy, N., & Malinin, A. (2020). Mathematical simulation of forest fire impact on industrial facilities and wood-based buildings. *Sustainability*, 12(13), 5475.
- Bergman, T. L., Bergman, T. L., Incropera, F. P., Dewitt, D. P., & Lavine, A. S. (2011). *Fundamentals of heat and mass transfer*. John Wiley & Sons.
- Bergman, T. L., Bergman, T. L., Incropera, F. P., Dewitt, D. P., & Lavine, A. S. (2011). *Fundamentals of heat and mass transfer*. John Wiley & Sons.
- Beyer, W. H. *CRC Standard Mathematical Tables*, 30th ed. Boca Raton, FL: CRC Press, pp. 695-697, 1996.
- Ceylan, H. T., & Myers, G. E. (1980). Long-time solutions to heat-conduction transients with time-dependent inputs.
- EnergyPlus Version 9.6.0 Documentation, Engineering Reference (2021). [https://energyplus.net/assets/nrel\\_custom/pdfs/pdfs\\_v9.6.0/EngineeringReference.pdf](https://energyplus.net/assets/nrel_custom/pdfs/pdfs_v9.6.0/EngineeringReference.pdf). Accessed 30 March 2021
- G.N. Walton, *Passive Solar Extension of the Building Loads Analysis and System Thermodynamics (BLAST) Program*, Technical Report, United States Army Construction Engineering Research Laboratory, Champaign, IL, 1981.
- Hénon, A., Mestayer, P. G., Lagouarde, J. P., & Voogt, J. A. (2012). An urban neighborhood temperature and energy study from the CAPITOUL experiment with the SOLENE model. *Theoretical and Applied Climatology*, 110(1), 177-196.
- Hillel, D. (1982). *Introduction to soil physics* New York, Academic Press (No. 631.43 H54).
- Hoff, S. J., & Janni, K. A. (1989). Monte Carlo technique for the determination of thermal radiation shape factors. *Transactions of the ASAE*, 32(3), 1023-1028.
- Howell, J. R. (1998). *The Monte Carlo method in radiative heat transfer*.
- Idczak, M., Groleau, D., Mestayer, P., Rosant, J. M., & Sini, J. F. (2010). An application of the thermo-radiative model SOLENE for the evaluation of street canyon energy balance. *Building and Environment*, 45(5), 1262-1275.

- Kanda, M., Kawai, T., Kanega, M., Moriwaki, R., Narita, K., & Hagishima, A. (2005). A simple energy balance model for regular building arrays. *Boundary-Layer Meteorology*, 116(3), 423-443
- Kim, H. J., & Lilley, D. G. (2002). Heat release rates of burning items in fires. *Journal of propulsion and power*, 18(4), 866-870.
- Kim, M. Y., Baek, S. W., & Park, J. H. (2001). Unstructured finite-volume method for radiative heat transfer in a complex two-dimensional geometry with obstacles. *Numerical Heat Transfer: Part B: Fundamentals*, 39(6), 617-635.
- Kramers, H. (1946). Heat transfer from spheres to flowing media. *physica*, 12(2-3), 61-80.
- Krayenhoff, E. S., & Voogt, J. A. (2007). A microscale three-dimensional urban energy balance model for studying surface temperatures. *Boundary-Layer Meteorology*, 123(3), 433-461.
- Lawrence Berkeley Laboratory (LBL), DOE2.1E-053 source code, 1994.
- Lee, D. I., & Lee, S. H. (2020). The Microscale Urban Surface Energy (MUSE) Model for Real Urban Application. *Atmosphere*, 11(12), 1347.
- Lin, S., Huang, X., Urban, J., McAllister, S., & Fernandez-Pello, C. (2019). Piloted ignition of cylindrical wildland fuels under irradiation. *Frontiers in Mechanical Engineering*, 54.
- Liu J, Luo Z, Zhao T, Shui J (2012) Ventilation in a street canyon under diurnal heating conditions. *International Journal of Ventilation*, 11(2), 141-154
- M. Yazdaniyan, J.H. Klems, Measurement of the exterior convective film coefficient for windows in low-rise buildings, *ASHRAE Transactions* 100 (Part 1)(1994).
- Mazumder, S., & Ravishankar, M. (2012). General procedure for calculation of diffuse view factors between arbitrary planar polygons. *International journal of heat and mass transfer*, 55(23-24), 7330-7335.
- Miguet, F., & Groleau, D. (2002). A daylight simulation tool for urban and architectural spaces—application to transmitted direct and diffuse light through glazing. *Building and environment*, 37(8-9), 833-843.
- Mills, G. (1997). An urban canopy-layer climate model. *Theoretical and applied climatology*, 57(3), 229-244.
- Mindykowski, P., Fuentes, A., Consalvi, J. L., & Porterie, B. (2011). Piloted ignition of wildland fuels. *Fire Safety Journal*, 46(1-2), 34-40.
- Mirhosseini, M., & Saboonchi, A. (2011). View factor calculation using the Monte Carlo method for a 3D strip element to circular cylinder. *International communications in heat and mass transfer*, 38(6), 821-826.
- Mitalas, G.P., and D.G. Stephenson. 1967. Room Thermal Response Factors. *ASHRAE Transactions* 73(1): 2.1-2.10.
- NOAA. NOAA Solar Calculator. 2018. Available online: <https://gml.noaa.gov/grad/solcalc/calcdetails.html> (accessed on 14 Aug 2021)

- Nusselt, W., & Jürges, W. (1922). Die Kühlung einer ebenen Wand durch einen Luftstrom (The cooling of a plane wall by an air flow). *Gesundheits Ingenieur*, 52(45), 641-642.
- Palyvos, J. A. (2008). A survey of wind convection coefficient correlations for building envelope energy systems' modeling. *Applied thermal engineering*, 28(8-9), 801-808.
- Ranz, W. E. (1952). Evaporation from drops, Parts I & II. *Chem Eng Prog.*, 48, 141-146.
- Rao, V. R., & Sastri, V. M. K. (1996). Efficient evaluation of diffuse view factors for radiation. *International journal of heat and mass transfer*, 39(6), 1281-1286.
- Rivera, J., Hernández, N., Consalvi, J. L., Reszka, P., Contreras, J., & Fuentes, A. (2021). Ignition of wildland fuels by idealized firebrands. *Fire Safety Journal*, 120, 103036.
- Rowley, F. B., Algren, A. B., & Blackshaw, J. L. (1930a). Effects of air velocity on surface coefficients. *ASHRAE Transactions*, 36, 123-136.
- Rowley, F. B., Algren, A. B., & Blackshaw, J. L. (1930b). Surface conductances as affected by air velocity, temperature and character of surface. *ASHRAE Trans*, 36, 429-446.
- Sánchez Tarifa, C., Pérez del Notario Martínez de Marañón, P., García Moreno, F., & Rodríguez Villa, A. (1967). Transport and Combustion of Firebrands. Final Report of Grants FG-SP-114 and FG-SP-146 Vol. II.
- Seem, J. E. (1987). Modeling of heat transfer in buildings (Doctoral dissertation, The University of Wisconsin-Madison).
- Seem, J. E. 1987. Modeling of Heat Transfer in Buildings, Ph.D. Thesis, University of Wisconsin, Madison, WI.
- Sparrow, E. M. (1963). A new and simpler formulation for radiative angle factors.
- Sparrow, E. M., Ramsey, J. W., & Mass, E. A. (1979). Effect of finite width on heat transfer and fluid flow about an inclined rectangular plate.
- Stephenson, D. G., & Mitalas, G. P. (1971). Calculation of heat conduction transfer functions for multi-layers slabs. *Air Cond. Engrs. Trans;(United States)*, 77.
- Tse, S. D., & Fernandez-Pello, A. C. (1998). On the flight paths of metal particles and embers generated by power lines in high winds--a potential source of wildland fires. *Fire Safety Journal*, 30(4), 333-356.
- Voogt, J. A., & Grimmond, C. S. B. (2000). Modeling surface sensible heat flux using surface radiative temperatures in a simple urban area. *Journal of Applied Meteorology and Climatology*, 39(10), 1679-1699.
- W.H. McAdams, *Heat Transmission*, third ed., McGraw-Hill Kogakusha, Tokyo, Japan, 1954, p. 249.
- Walton, G. N. (1983). Thermal analysis research program reference manual. National Bureau of Standards, March.
- Wang, S., Ding, P., Lin, S., Gong, J., & Huang, X. (2021). Smoldering and Flaming of Disc Wood Particles Under External Radiation: Autoignition and Size Effect. *Frontiers in Mechanical Engineering*, 65.



- Wu, L. (1995). An urban canopy layer surface energy balance climate model (Doctoral dissertation, Ph. D. Dissertation, University of California, Los Angeles).
- Yaghoobian, N., & Kleissl, J. (2012). An indoor–outdoor building energy simulator to study urban modification effects on building energy use—Model description and validation. *Energy and Buildings*, 54, 407-417.
- Yang, X., & Li, Y. (2013). Development of a three-dimensional urban energy model for predicting and understanding surface temperature distribution. *Boundary-layer meteorology*, 149(2), 303-321.
- Young Byun, D., Wook Baek, S., & Young Kim, M. (2003). Investigation of radiative heat transfer in complex geometries using blocked-off, multiblock, and embedded boundary treatments. *Numerical Heat Transfer: Part A: Applications*, 43(8), 807-825.
- Zabihi, M., Lari, K., & Amiri, H. (2017). Coupled radiative-conductive heat transfer problems in complex geometries using embedded boundary method. *Journal of the Brazilian Society of Mechanical Sciences and Engineering*, 39(7), 2847-2864.